Supporting Information for

Experimental Observation of Altermagnetism in Twisted $CrPS_4$ van der Waals Homostructures

Junying Chen[1,2†], Xing Xie[1,2†], Shaofei Li[1], Siyu Zhang[1,2], Shikun Hou[1,2], Xian Zhang[1,2], Jun He[1], Zongwen Liu[3,4], Jian-Tao Wang[5,6,7], and Yanping Liu[1,2,8*]

1. *Institute of Quantum Physics, School of Physics, Central South University, 932 South Lushan Road, Changsha, Hunan 410083, People's Republic of China*
2. *State Key Laboratory of Precision Manufacturing for Extreme Service Performance, Central South University, 932 South Lushan Road, Changsha, Hunan 410083, People's Republic of China*
3. *School of Chemical and Biomolecular Engineering, The University of Sydney, NSW 2006, Australia*
4. *The University of Sydney Nano Institute, The University of Sydney, NSW 2006 Australia*
5. *Beijing National Laboratory for Condensed Matter Physics, Institute of Physics, Chinese Academy of Sciences, Beijing 100190, People's Republic of China*
6. *School of Physical Sciences, University of Chinese Academy of Sciences, Beijing 100049, People's Republic of China*
7. *Songshan Lake Materials Laboratory, Dongguan, Guangdong 523808, People's Republic of China*
8. *Shenzhen Research Institute of Central South University, Shenzhen 518000, People's Republic of China*

† These authors contributed equally to this work.

* Correspondence and requests for materials should be addressed to email: liuyanping@csu.edu.cn

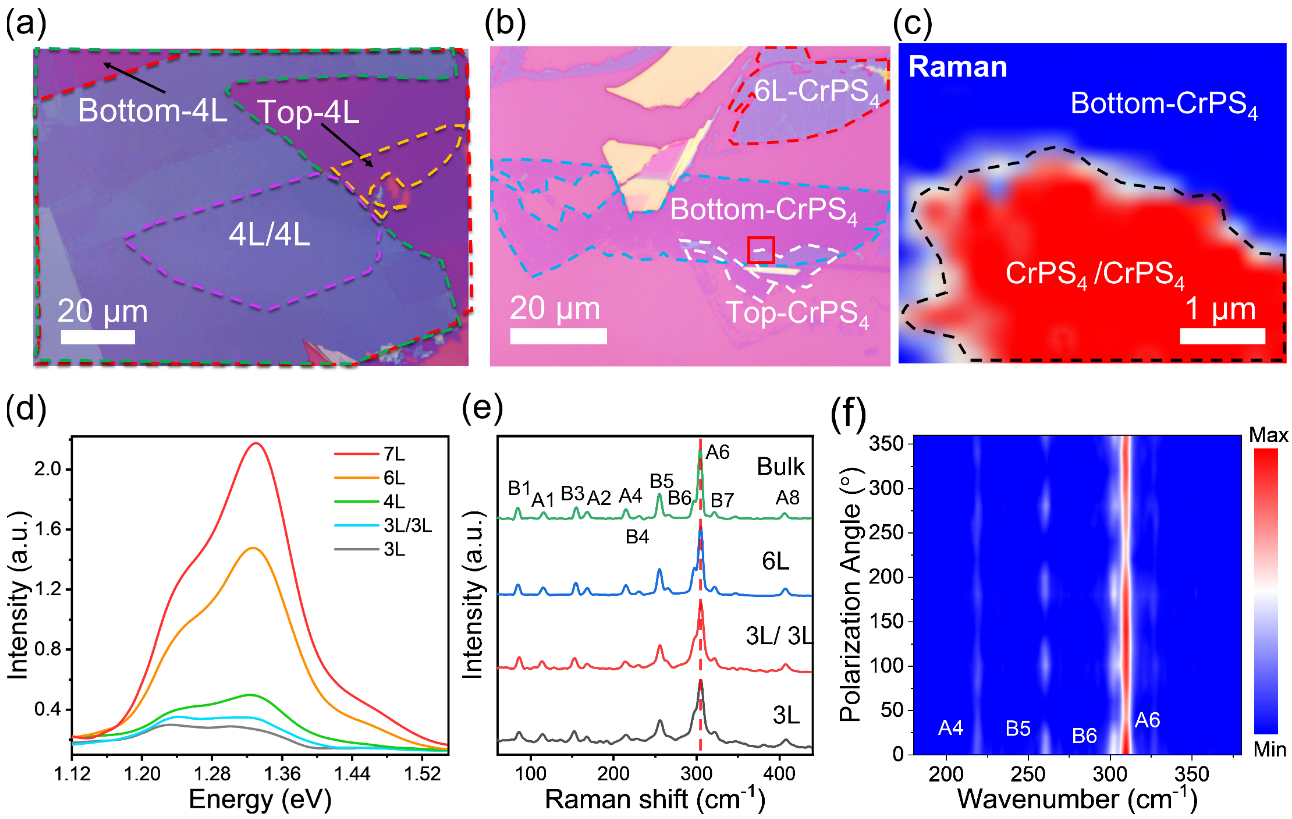

Figure S1. Samples and optical characteristics of 90°-$CrPS_4$/$CrPS_4$ and 1.5°-$CrPS_4$/$CrPS_4$. a, Optical image of 90°-$CrPS_4$/$CrPS_4$ samples. The red and green dotted frames represent the top and bottom $CrPS_4$ layers, respectively. **b**, Optical image of the 1.5°-$CrPS_4$/$CrPS_4$ samples. The white and blue dashed line outlines the top and bottom $CrPS_4$ layers, respectively. **c**, Raman mapping of 1.5°-$CrPS_4$/$CrPS_4$ samples with scanning region marked by the red box in (**b**). The red and blue regions denote the stronger and weaker Raman intensity corresponding to the 1.5°-$CrPS_4$/$CrPS_4$ and bottom $CrPS_4$, respectively. **d**, PL spectra of 3L, 4L, 6L, 7L and 1.5°-3L/3L $CrPS_4$ measured at room temperature, revealing increasing PL intensity with increasing the layer number of $CrPS_4$. **e**, Raman spectra of 3L, 6L, bulk, and 1.5°-3L/3L $CrPS_4$ measured at room temperature. **f**, Color plots of polarization Raman spectra of 1.5°-3L/3L, illustrating the strong periodic Raman intensity with the laser polarization angle.

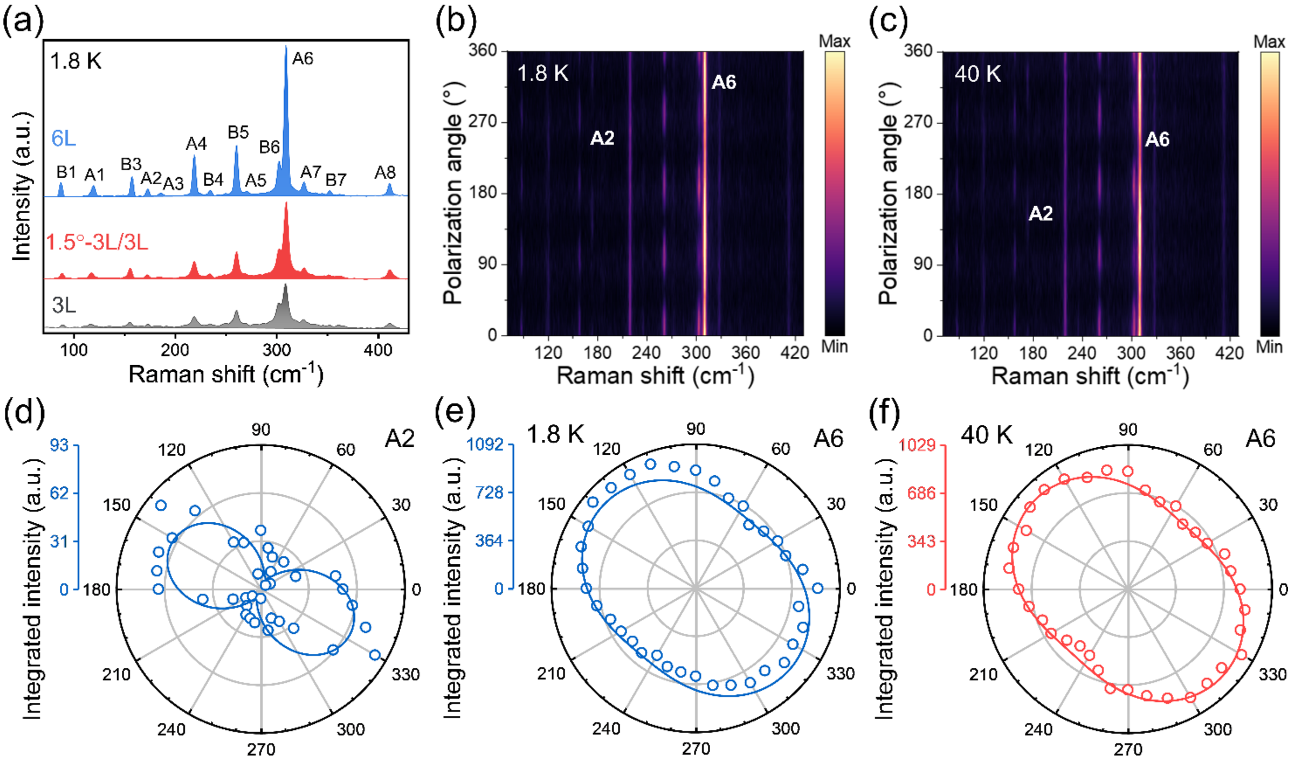

Figure S2. Polarization Raman characteristics of 1.5°-3L/3L. a, Raman spectra of 3L, 1.5°-3L/3L, and 6L $CrPS_4$ measured at 1.8 K. **b-c**, Polarization Raman of 1.5°-3L/3L in color plots at 1.8 K (**b**) and 40 K (**c**), revealing the significant polarization dependence. **d**, Polar plots of Raman intensity for A2 mode of 1.5°-3L/3L. **e-f**, Polarization-resolved Raman intensity for A6 mode of 1.5°-3L/3L at 1.8 K (**e**) and 40 K (**f**). The polarization axis of A6 mode along ~140° both at 1.8 K and 40 K, indicating that the magnetic order transition from ferromagnetic to paramagnetic do not arise the variation in polarization angle.

Note 1: Polarization-Dependent Raman and Photoluminescence of 90°-$CrPS_4$/$CrPS_4$

The A6 Raman mode of $CrPS_4$ exhibits pronounced two-fold anisotropy arising from the anisotropic crystal structure along the a and b axes.[1-3] In an orthogonally stacked configuration, the polarization axes of the top and bottom $CrPS_4$ layers are expected to be mutually perpendicular, leading to orthogonal Raman scattering responses. In our measurements, the polarization dependence of the A6 mode in the 90°-3L/4L and 90°-5L/4L heterostructures becomes markedly weaker, yielding nearly isotropic Raman patterns. As the thickness difference between the top and bottom layers increases, the overall anisotropy persists but develops a secondary maximum perpendicular to the primary polarization axis. This evolution from anisotropy to isotropy is attributed to the orthogonal stacking geometry of the two $CrPS_4$ layers.

Differences in light absorption, emission, and scattering between the top and bottom $CrPS_4$ layers result in non-uniform optical intensities. The mismatch in their polarized responses leads to partial cancellation of anisotropic contributions. Consequently, in 90°-3L/4L and 90°-5L/4L, the superposition of the polarization-dependent Raman intensities from the two layers produces an overall response that is nearly independent of the laser polarization (Figure S3a–b). With larger layer-number differences, this isotropy diminishes because the intensity imbalance between the top and bottom layers reduces the degree of overlap, as shown in Figure S3c.

In contrast, the symmetric 90°-4L/4L heterostructure displays distinct vibrational features not observed in asymmetric stacks. In this case, the A6 Raman mode does not appear as a simple superposition of two overlapping peaks. Instead, altermagnetic interlayer coupling induces opposite frequency shifts for the top and bottom $CrPS_4$ layers relative to the intrinsic A6 position, resulting in two separate components. The polarization behavior of these split modes preserves the anisotropic characteristics of their respective layers ($A6_1$ from the top layer and $A6_2$ from the bottom layer; see main text).

For polarized photoluminescence (PL), the 90°-4L/4L heterostructure exhibits behavior consistent with the layer-dependent polarization in orthogonal stacking. The PL intensity superposition from the two layers closely reproduces the experimentally measured polarization-resolved PL spectra of 90°-4L/4L (Figure S4a). As the difference in layer number increases, the degree of PL polarization also increases (Figure S4). Among our measured samples, the 90°-6L/4L structure exhibits the largest polarization anisotropy in PL emission.

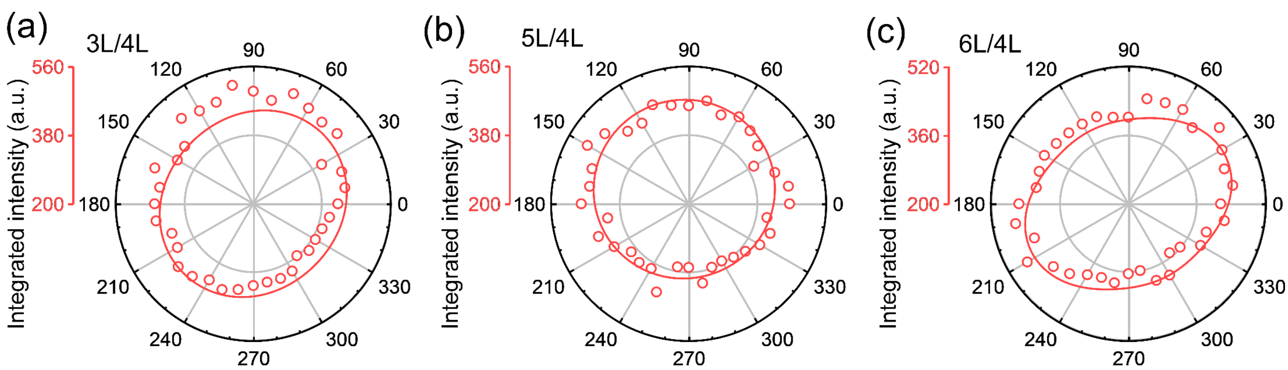

Figure S3. Polarization Raman of asymmetry 90°-$CrPS_4$/$CrPS_4$ for A6 mode. a-c, Polar plots of Raman intensity for 90°-3L/4L (a), 90°-5L/4L (b), and 90°-6L/4L (c). Hollow dots and solid curves represent the experimental data and fitting results, respectively. The polarization Raman intensity shows weak anisotropy in 90°-3L/4L and 90°-5L/4L, while 90°-6L/4L exhibits four-leaves polarization pattern with long axis along ~30° and secondary maximum along ~120°.

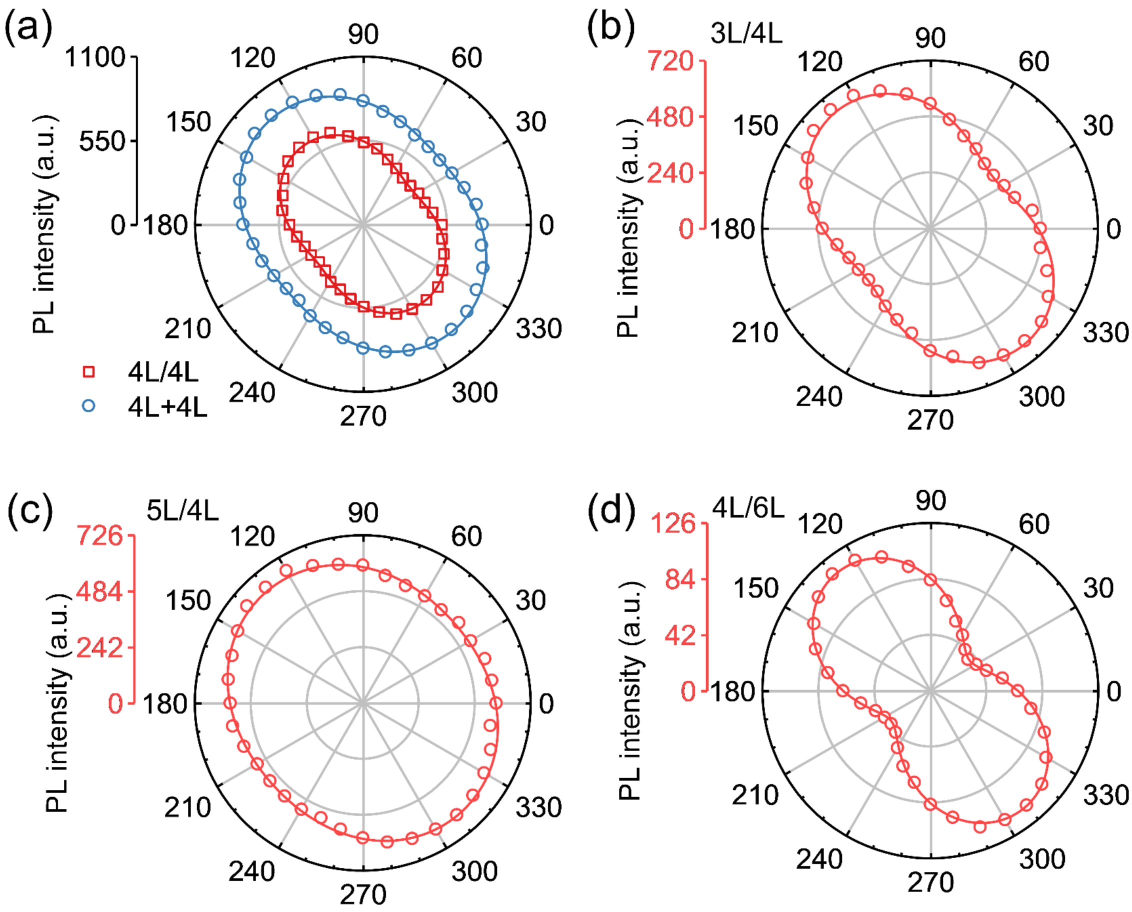

Figure S4. Polarization PL characteristic of 90°-$CrPS_4$/$CrPS_4$. a-d, Polarization-dependent Raman intensity of P1 peak for 90°-4L/4L (**a**), 90°-3L/4L (**b**), 90°-5L/4 L (**c**), and 90°-4L/6L (**d**). All samples show consistent polarization angle along ~130°. With increasing the layers, the degree of linear polarization (DOLP) first decreases and then increases, due to the thickness difference between top and bottom layers firstly decreasing and then increasing. For orthogonal stacking anisotropic materials, polarization axis of top layer is orthogonal to that of bottom layer, theoretically resulting in the four-fold period polarization Raman and PL. However, experimental differences in optical absorption and emissions arise the difference in PL intensity, which leads to two-fold polarization intensity with reduced DOLP.

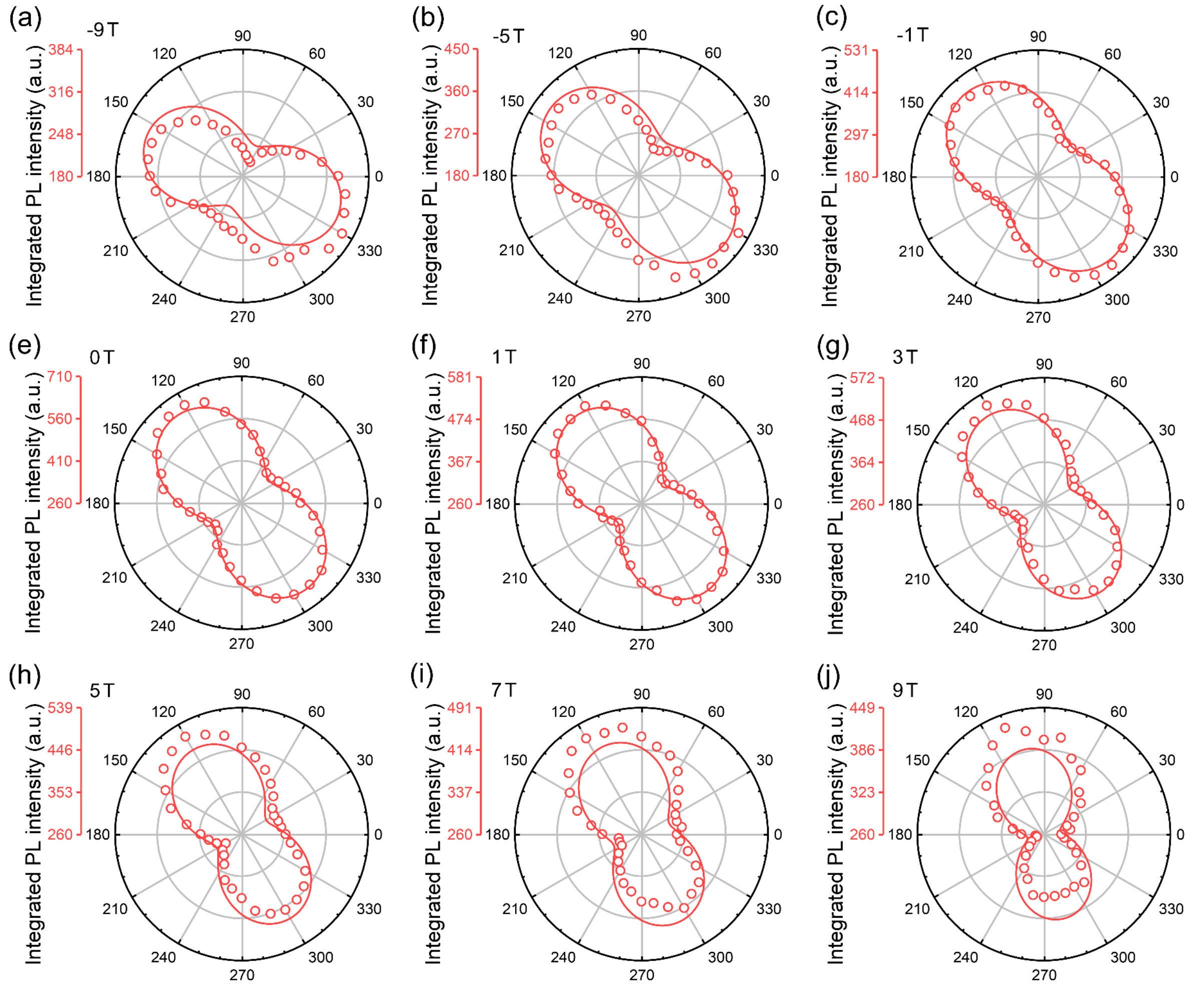

Figure S5. Polarization PL intensity of 90°-4L/4L under magnetic fields. a-j, Polar plots of PL intensity of 90°-4L/4L under selected magnetic field. Hollow points and solid curves are the extracted data from PL spectra of 90°-4L/4L and fitting results, respectively. With varying the magnetic field, the polarization axis changes, with anticlockwise and clockwise rotation for negative and positive magnetic field, respectively.

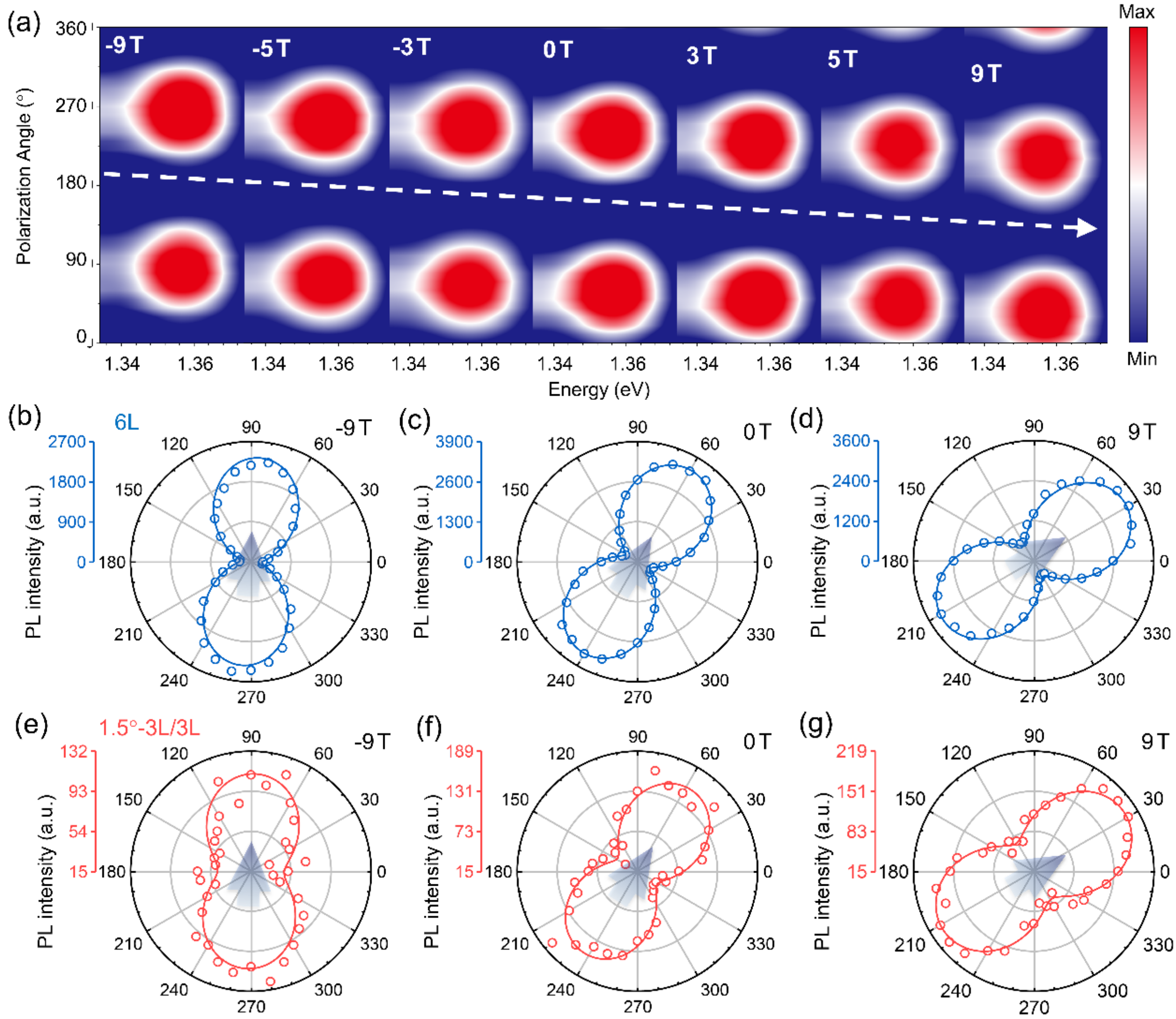

Figure S6. Polarization-dependent PL spectra of 1.5°-3L/3L and 6 L $CrPS_4$ under magnetic field. **a**, Color plots of polarization-resolved PL spectra for 1.5°-3L/3L under selected magnetic field, revealing the deflected polarization axis. **b-d**, Polar plots of PL intensity for 6L $CrPS_4$. **e-f**, Polar plots of PL intensity for 1.5°-3L/3L. Hollow dots and solid curves represent the experimental data and fitting results, respectively. The grey arrows denote the polarization axis direction, illustrating the varying polarization axis under magnetic field, attributed to the rotation of dipole moment vector induced by the magnetic field.

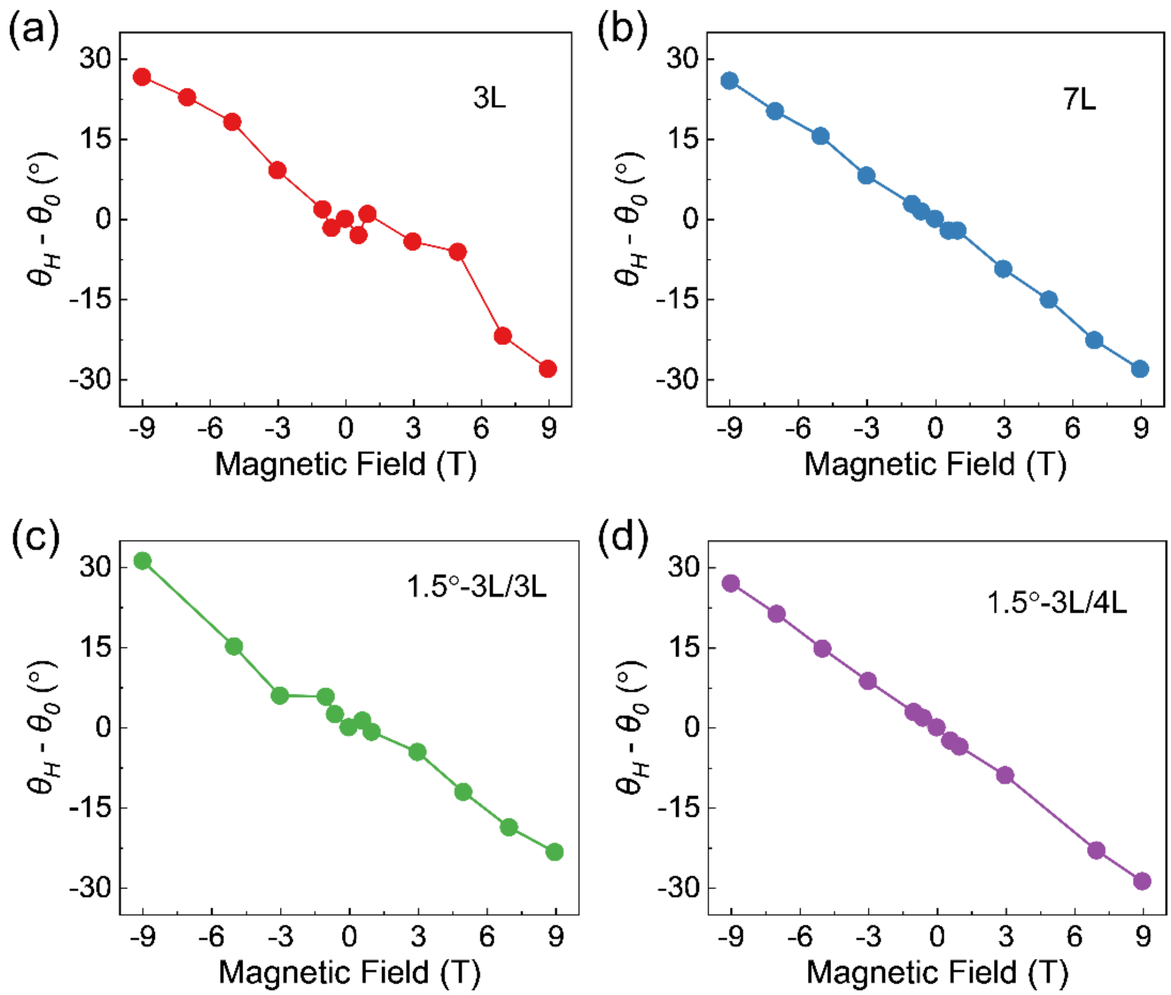

Figure S7. Polarization angle of polarization PL intensity. a-d, Normalized polarization angle as a function of magnetic field. The polarization angle under magnetic field is normalized to the polarization angle at 0 T, i.e. θ_H-θ_0, where θ_H and θ_0 represent the polarization angle measured under magnetic field and at 0 T, respectively. The polarization angle shows nearly linear decrease as the magnetic field changes from -9 T to 9 T for all samples. This indicates that magnetic-field-induced rotation of polarization axis is independent on the magnetic orders of $CrPS_4$.

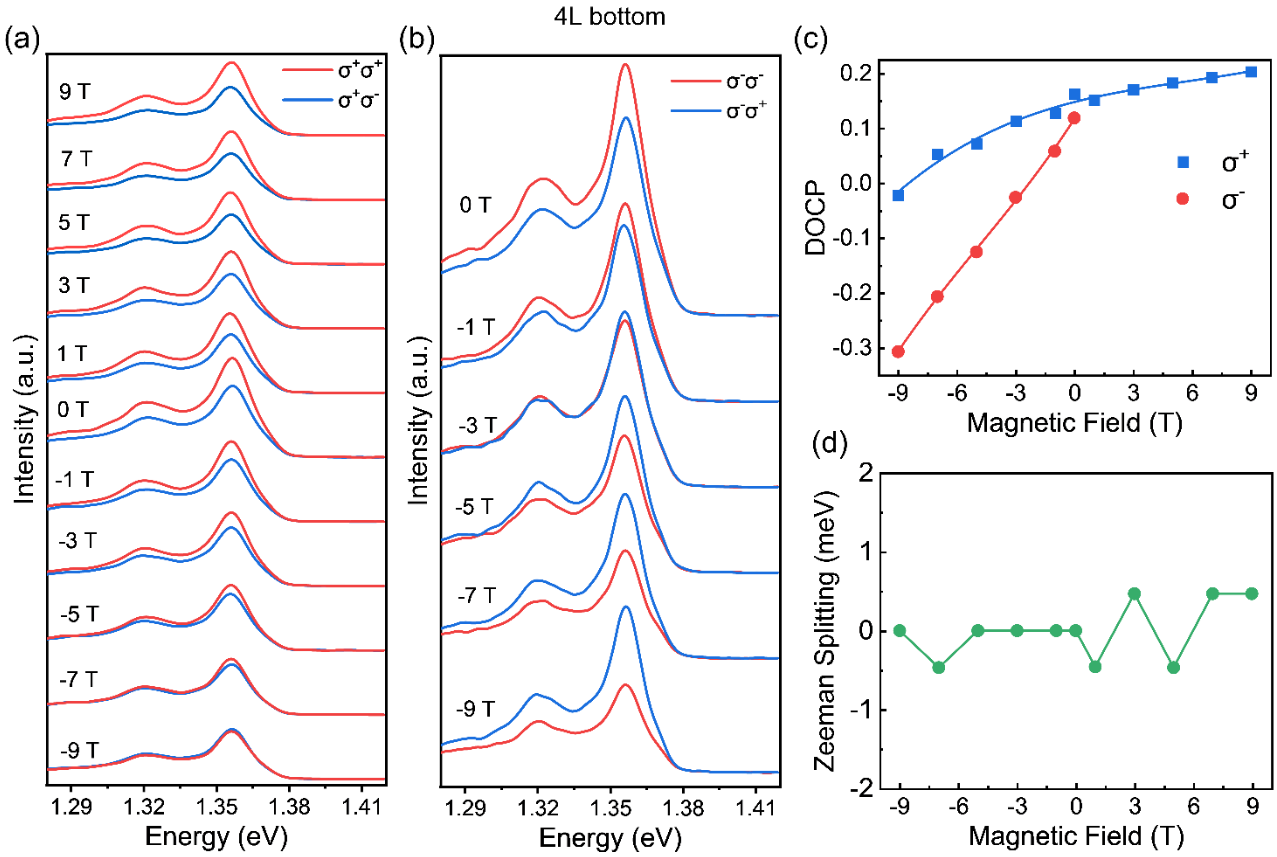

Figure S8. Circular polarization spectra and Zeeman splitting for bottom 4L $CrPS_4$. a-b, Circularly polarized PL spectra of bottom 4L $CrPS_4$ under selected magnetic field at σ^+ (**a**) and σ^- (**b**) excitation. The red and blue curves represent the symmetry and asymmetry excitation and emission, respectively. **c**, Degree of circular polarization (DOCP) as a function of magnetic field for bottom 4L $CrPS_4$. As the magnetic field changes from -9 T to 9 T, the magnetic-field-dependent DOCP shows increasing trend both at σ^+ (blue) and σ^- (red) excitation, with slow and fast variation for σ^+ and σ^- excitation, respectively. **d**, Zeeman splitting energy as a function of magnetic field for bottom 4L $CrPS_4$, calculated by $\Delta E = E(\sigma^+) - E(\sigma^-)$, where $E(\sigma^+)$ and $E(\sigma^-)$ are the PL energy at σ^+ and σ^- emissions, respectively. The Zeeman splitting energy exhibits near zero under magnetic field, suggesting the negligible Zeeman splitting in bottom 4L $CrPS_4$.

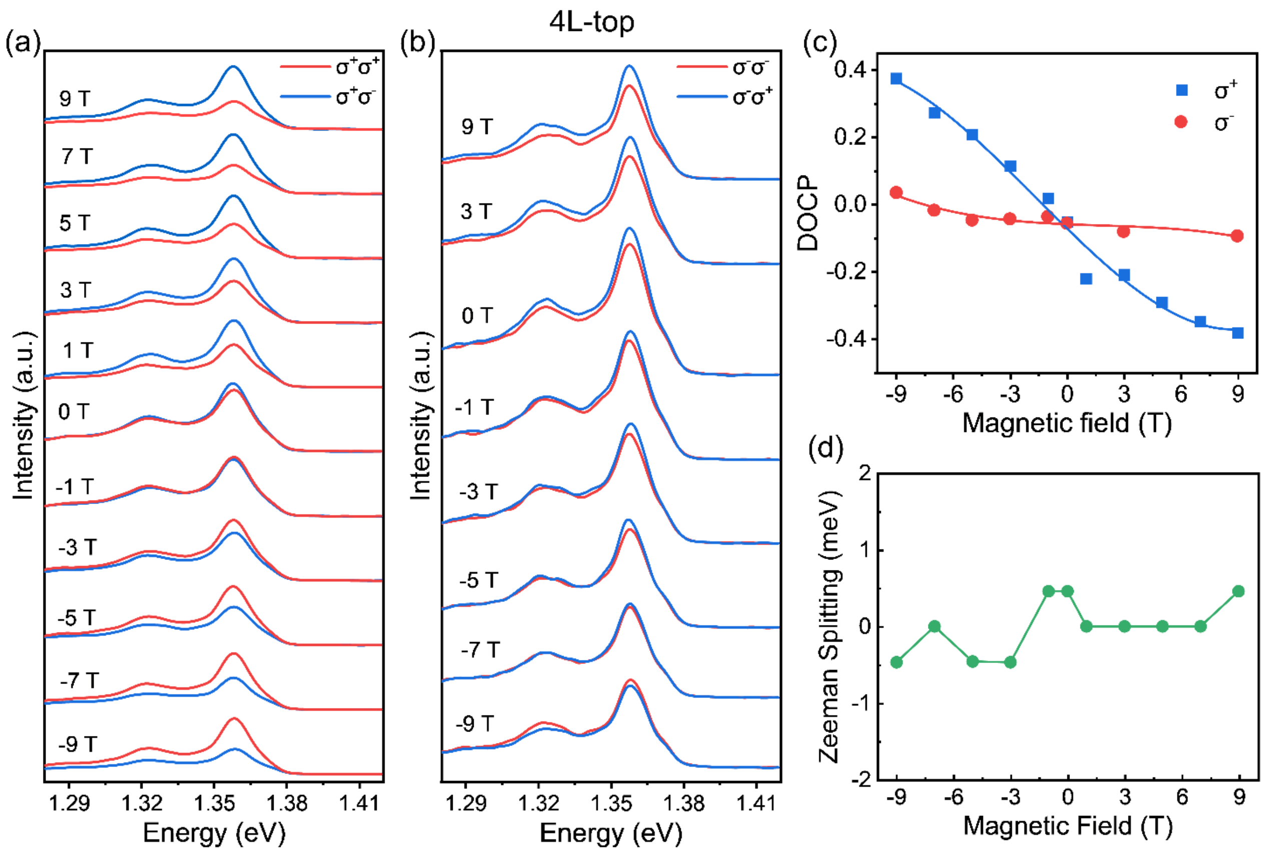

Figure S9. Circular polarization spectra and Zeeman splitting for top 4L $CrPS_4$. a-b, Circular polarization PL spectra of top 4L $CrPS_4$ under selected magnetic field at σ^+ (**a**) and σ^- (**b**) excitation. The PL intensity for σ^+/σ^+ is higher than those for σ^+/σ^- under negative magnetic field, while they exhibit lower PL intensity compared to those for σ^+/σ^- under positive magnetic field. For σ^- excitation, PL intensity for σ^-/σ^+ is stronger than those σ^-/σ^- under magnetic field except for -9 T. **c**, DOCP as a function of magnetic field for top 4L $CrPS_4$. With changing the magnetic field from -9 T to 9 T, the magnetic-field-dependent DOCP exhibits decreasing trend both at σ^+ (blue) and σ^- (red) excitation, with fast and slow variation for σ^+ and σ^- excitation, respectively. This is opposite to the bottom 4L $CrPS_4$. **d**, Zeeman splitting energy as a function of magnetic field for top 4L $CrPS_4$. The Zeeman splitting energy exhibits near zero under magnetic field, suggesting the negligible Zeeman splitting in top 4L $CrPS_4$.

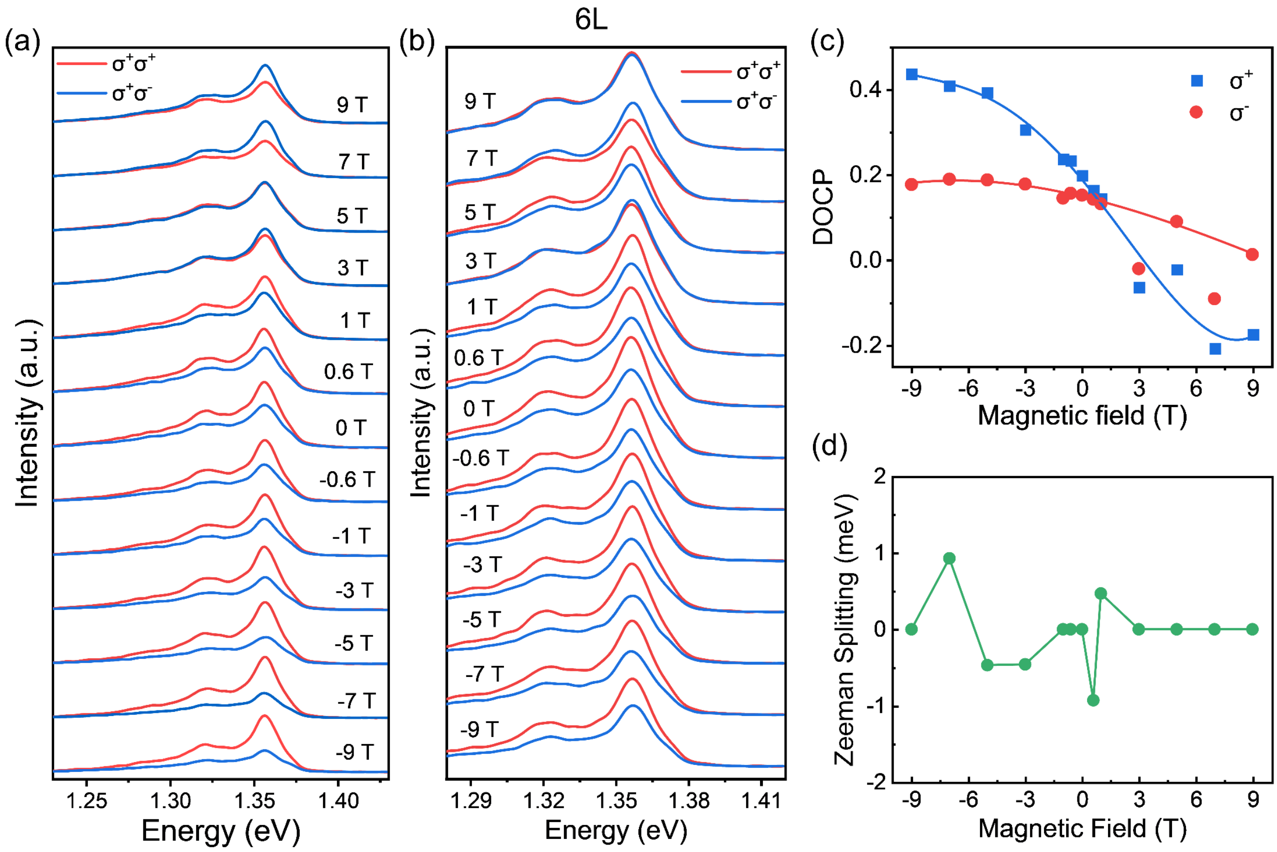

Figure S10. Circular polarization spectra and Zeeman splitting for 6L $CrPS_4$. a-b, Circular polarization PL spectra of 6L $CrPS_4$ under selected magnetic field at σ^+ (**a**) and σ^- (**b**) excitation. **c**, DOCP as a function of magnetic field for 6L $CrPS_4$. As the magnetic field changes from -9 T to 9 T, the magnetic-field-dependent DOCP exhibits decreasing trend both at σ^+ (blue) and σ^- (red) excitation, with fast and slow variation for σ^+ and σ^- excitation, respectively. This suggests the homodromous magnetic-field-dependent DOCP for σ^+ and σ^- excitation in antiferromagnetic $CrPS_4$. **d**, Zeeman splitting energy as a function of magnetic field for bottom $CrPS_4$. The Zeeman splitting energy exhibits near zero under magnetic field, suggesting the negligible Zeeman splitting in 6L $CrPS_4$.

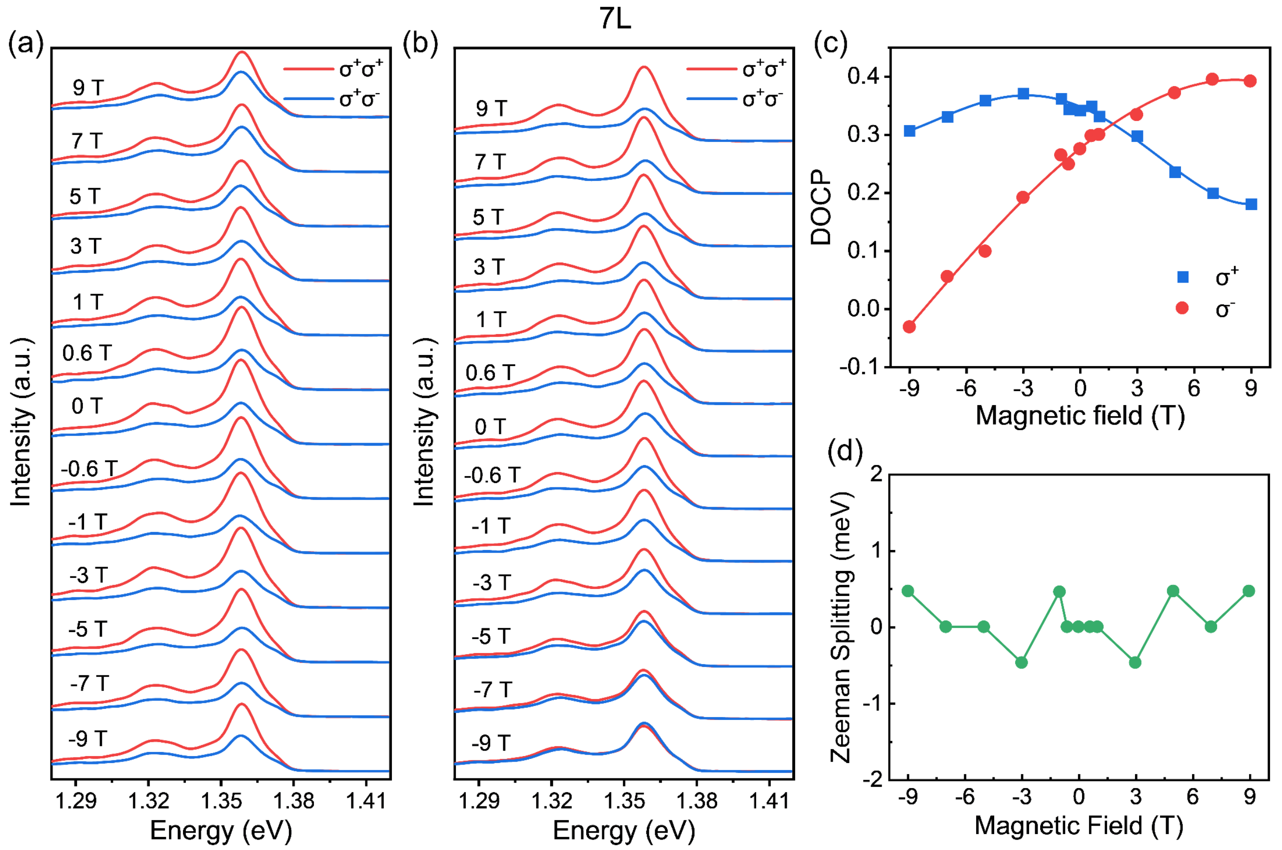

Figure S11. Circular polarization spectra and Zeeman splitting for 7L $CrPS_4$. a-b, Circular polarization PL spectra of 7L $CrPS_4$ under selected magnetic field at σ^+ (**a**) and σ^- (**b**) excitation. **c**, magnetic-field-dependent DOCP for 7L $CrPS_4$. As the magnetic field changes from -9 T to 9 T, the magnetic-field-dependent DOCP exhibits decreasing and increasing trend at σ^+ (blue) and σ^- (red) excitation, respectively. **d**, Zeeman splitting energy as a function of magnetic field for 7L $CrPS_4$. The Zeeman splitting energy fluctuates near zero under magnetic field, suggesting the negligible Zeeman splitting in 7L $CrPS_4$.

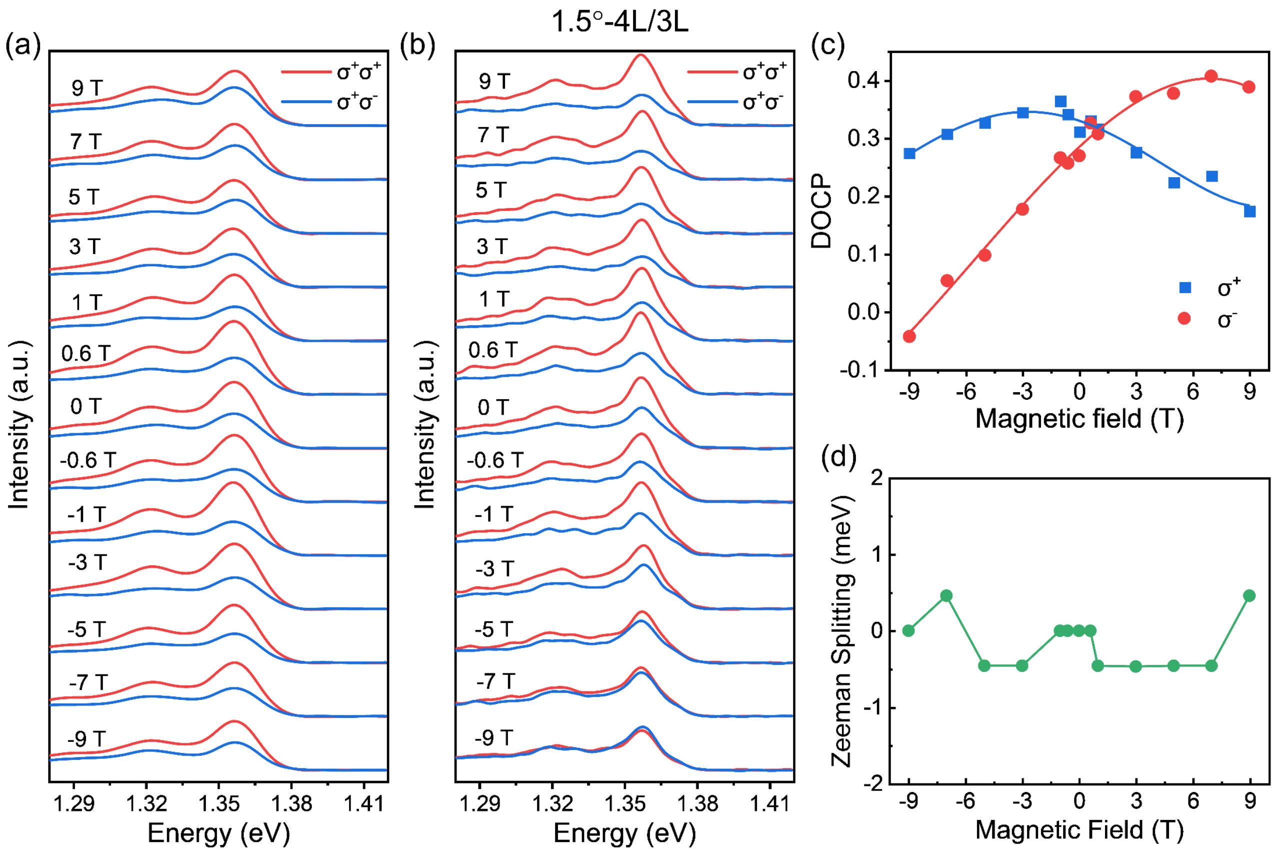

Figure S12. Circular polarization spectra and Zeeman splitting for 1.5°-3L/4L. a-b, Circular polarization PL spectra of 1.5°-3L/4L under selected magnetic field at σ^+ (**a**) and σ^- (**b**) excitation. **c**, magnetic-field-dependent DOCP for 1.5°-3L/4L. As the magnetic field changes from -9 T to 9 T, the magnetic-field-dependent DOCP exhibits decreasing and increasing trend at σ^+ (blue) and σ^- (red) excitation, respectively. This suggests the cross-changing magnetic-field-dependent DOCP for σ^+ and σ^- excitation in ferromagnetic $CrPS_4$. **d**, Zeeman splitting energy as a function of magnetic field for 1.5°-3L/4L. The Zeeman splitting energy fluctuates near zero under magnetic field, suggesting the negligible Zeeman splitting in 1.5°-3L/4L. Based on the Zeeman splitting of 4L, 6L, 7L, and 1.5°-3L/4L, both ferromagnetic and antiferromagnetic $CrPS_4$ exhibit negligible Zeeman effect, which is different from the significant Zeeman splitting observed in 90°-4L/4L. This implies the different magnetism between them.

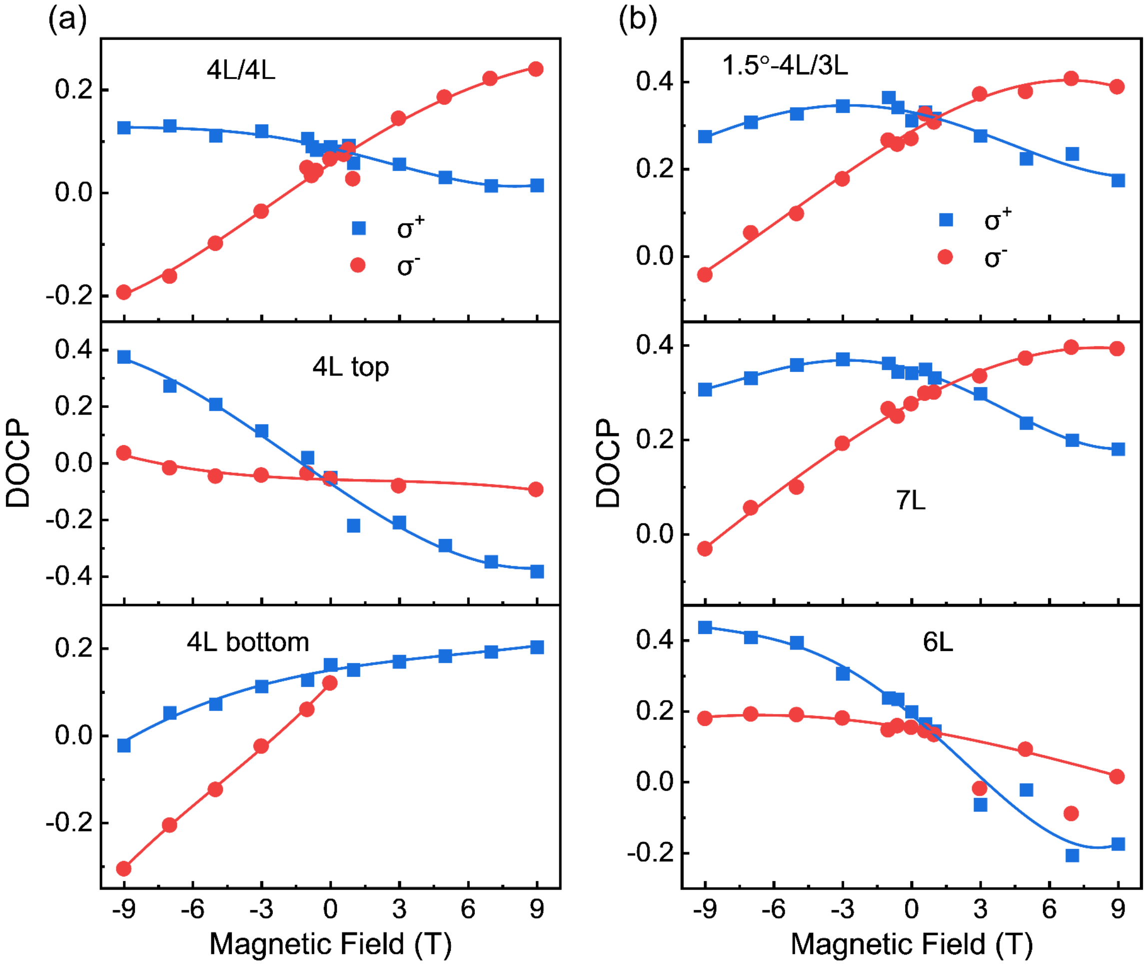

Figure S13. Magnetic-field-dependent DOCP for $CrPS_4$ systems. a, DOCP as a function of magnetic field for 90°-4L/4L (top panel), top (middle panel), and bottom (bottom panel) 4L $CrPS_4$. **b**, DOCP as a function of magnetic field for 1.5°-4L/3L (top panel), 7L (middle panel), and bottom (bottom panel) 6L $CrPS_4$. As the magnetic field changes from -9 T to 9 T, the magnetic-field-dependent DOCP shows homodromous varying trend both at σ^+ and σ^- excitation for top, bottom 4L, and 6L$CrPS_4$, while 1.5°-4L/4L and 7L $CrPS_4$ exhibits an increasing and decreasing DOCP at σ^- and σ^+ excitation, respectively. These indicate different DOCP behavior under magnetic field for ferromagnetic and antiferromagnetic CrPS4. Furthermore, 90°-4L/4L exhibits similar magnetic-field-dependent DOCP to 1.5°-4L/4L and 7L $CrPS_4$, demonstrating the ferromagnetism in 90°-4L/4L.

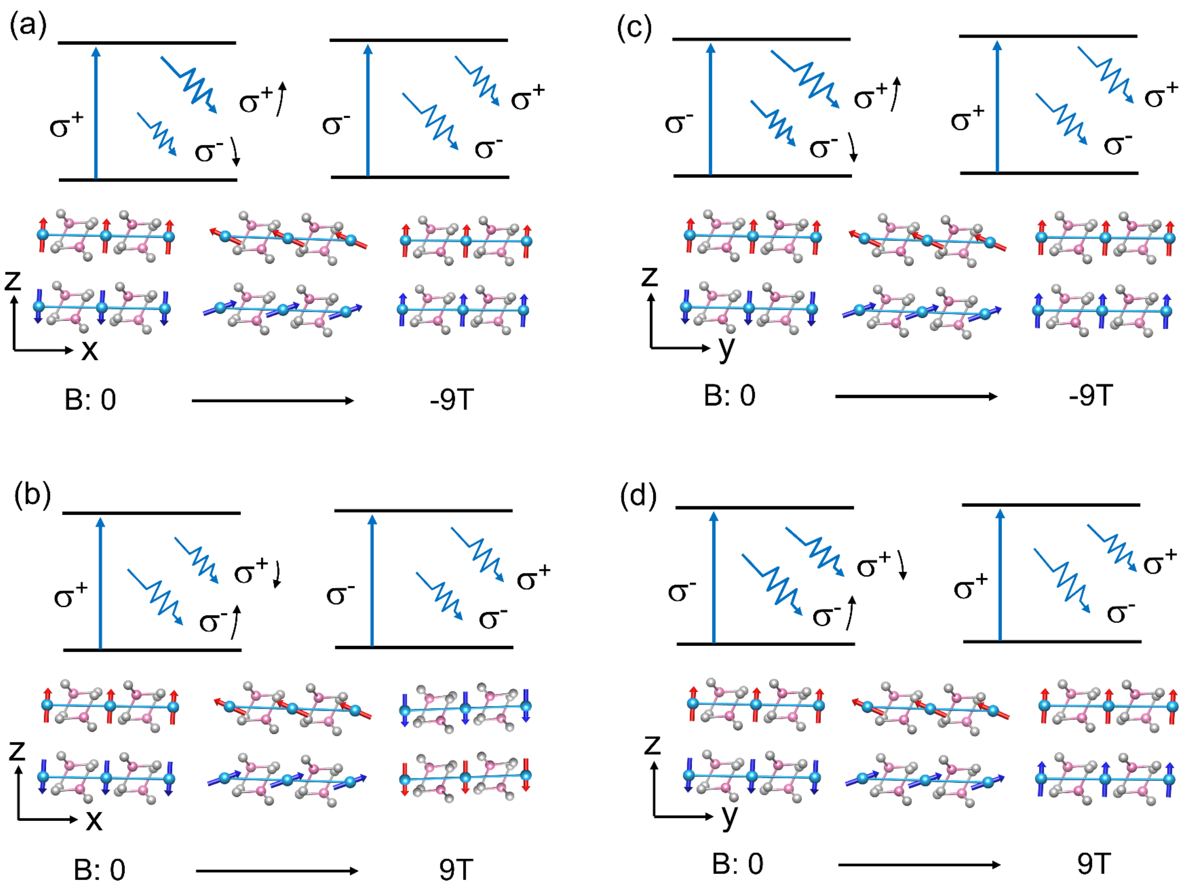

Figure S14. Mechanism of magnetic field-dependent DOCP in $CrPS_4$. a-d, Schematic diagram illustrating the circular polarization emission related to crystal orientation due to canted antiferromagnetic order under magnetic field. Lower panels are the magnetic orders. The coordinate axis represents the experimentally spatial coordinate axes.

Note 2. Magnetic-field-dependent DOCP

For antiferromagnetic (AFM) $CrPS_4$, the crystal-axis arrangement determines the coupling between circularly polarized light and the orientation of the canted magnetic order.[4] When the canted magnetic moments align along the experimental x-axis, AFM $CrPS_4$ couples predominantly with σ^+ circularly polarized excitation. Consequently, the variation in circular polarization under σ^+ excitation is more pronounced than that under σ^- excitation.

Under a negative magnetic field (B < 0), the σ^+ emission intensity increases with increasing field strength, whereas the σ^- emission decreases (Figure S13a). In contrast, under a positive magnetic field (B > 0), σ^+ emission weakens while σ^- emission strengthens (Figure S13b). This behavior leads to an increase in the degree of circular polarization (DOCP=$(I_{\sigma+/-}- I_{\sigma-/+}) /(I_{\sigma+/-}+I_{\sigma-/+})$ for $\sigma^{+/-}$ excitation, where $I_{\sigma+/-}$ denotes the PL intensity for $\sigma^{+/-}$ emission) under B < 0, and a decrease in DOCP under B > 0 for σ^+ excitation.

For σ^- excitation, the coupling to the canted magnetic order is weak; therefore, excitonic emission is only slightly affected by the magnetic field, resulting in a minimal change in DOCP. The modest enhancement of σ^+ emission and slight reduction of σ^- emission yield a mild overall decrease in DOCP as the magnetic field varies from −9 T to 9 T. When the canted magnetic moments align along the experimental y-axis, AFM $CrPS_4$ couples primarily with σ^- excitation, leading to an opposite DOCP trend (Figure S13c, d).

In the ferromagnetic (FM) phase of $CrPS_4$, the canted magnetic order vanishes. Under B < 0, σ^+ emission intensifies and σ^- emission weakens, producing an increasing and decreasing DOCP for σ^+ and σ^- excitation, respectively, as the field strength increases from 0 to −9 T. Conversely, for B > 0, σ^+ emission decreases while σ^- emission increases, leading to opposite DOCP trends as the field is swept from 0 to 9 T. Thus, the magnetic-field-dependent DOCP exhibits a decreasing trend for σ^+ excitation and an increasing trend for σ^- excitation as B varies from −9 T to 9 T. In the 90°-4L/4L configuration, the magnetic-field-dependent DOCP follows the ferromagnetic-type behavior, confirming the emergence of ferromagnetism in this heterostructure.

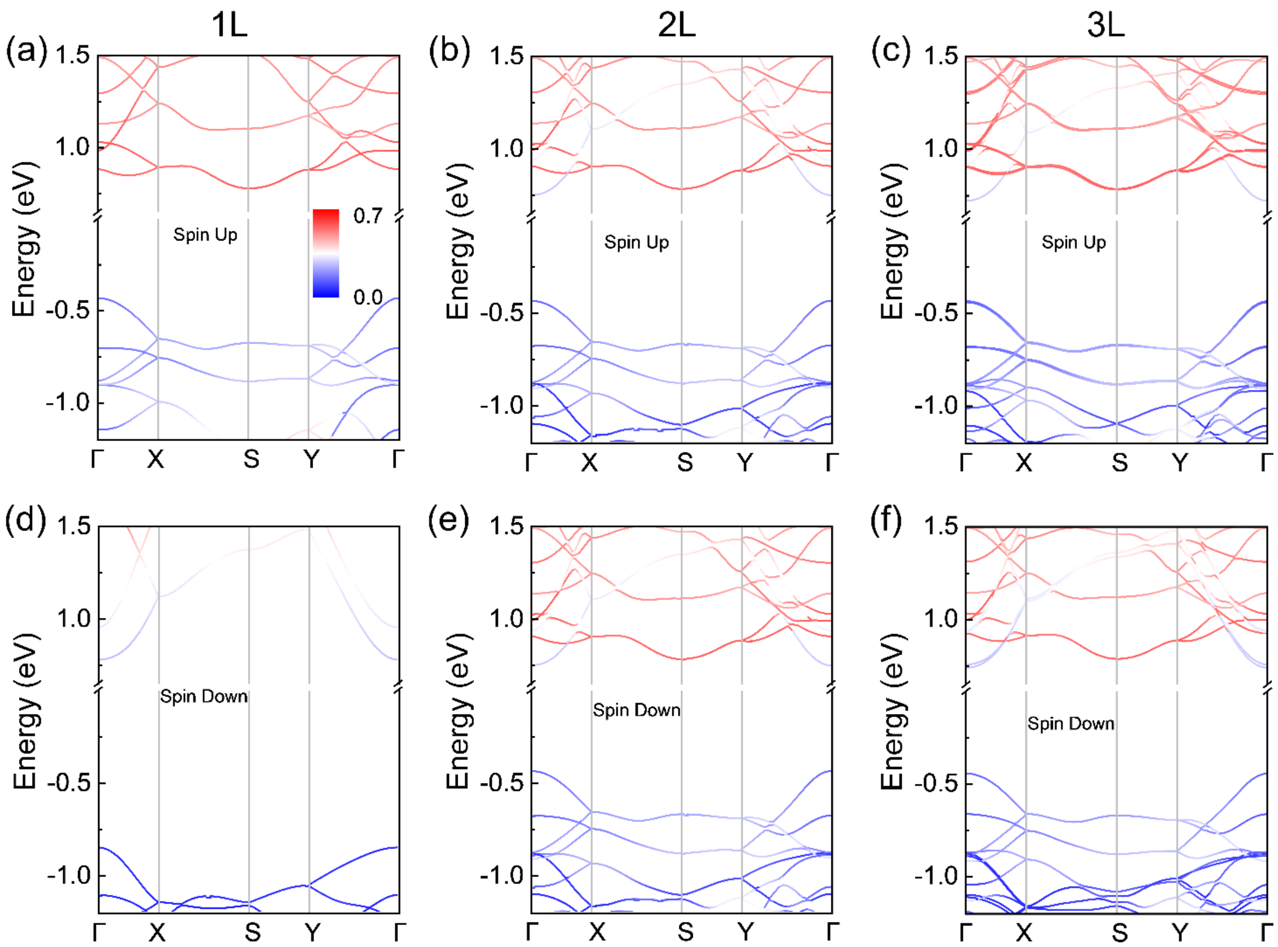

Figure S15. Calculated band structures of layer-dependent $CrPS_4$. a-c, Band structures of (**a**) 1L, (**b**) 2L, and (**c**) 3L $CrPS_4$ with spin up state. **d-e**, Band structures of (**d**) 1L, (**e**) 2L, and (**f**) 3L $CrPS_4$ with spin down state. The color mapping represents the Cr atom weight, with blue for low weight and red for high weight. The dispersion bands for 2L and 3L $CrPS_4$ exhibit similar behaviors both for spin up and down due to the A-type antiferromagnetic configuration. The difference between them is the spin splitting appeared in the 3L $CrPS_4$ compared to 2L $CrPS_4$. However, this spin splitting is minor near Fermi level, leading to the small different in optical transition for spin up and spin down. For 1L $CrPS_4$, the spin splitting is significant, arising the significantly different dispersion distributions for spin up and spin down.

References

1. Lee, J. *et al.* Structural and Optical Properties of Single- and Few-Layer Magnetic Semiconductor $CrPS_4$. *ACS Nano* **11**, 10935-10944 (2017).

2. Son, J. *et al.* Air-Stable and Layer-Dependent Ferromagnetism in Atomically Thin van der Waals $CrPS_4$. *ACS Nano* **15**, 16904-16912 (2021).

3. Huang, M. *et al.* Layer-Dependent Magnetism and Spin Fluctuations in Atomically Thin van der Waals Magnet $CrPS_4$. *Nano Lett.* **23**, 8099-8105 (2023).

4. Peng, Y. *et al.* Magnetic Structure and Metamagnetic Transitions in the van der Waals Antiferromagnet $CrPS_4$. *Adv. Mater.* **32**, 2001200 (2020).